Role of sample thickness and self-absorption effects in simultaneous XEOL-XAS measurements on single crystalline ZnO and GaN

Sergiu Levcenko,[1,2,*] Konrad Ritter,[1] Hans H. Falk,[1] Timo Pfeiffelmann,[1] Lukas Trefflich,[1] Edmund Welter,[2] Marius Grundmann,[1] and Claudia S. Schnohr[1]

[1]*Felix Bloch Institute for Solid State Physics, Leipzig University, Linnéstraße 5, 04103 Leipzig, Germany*

[2]*Deutsches Elektronen-Synchrotron DESY, Notkestrasse 85, D-22607 Hamburg, Germany*

(Received 9 January 2025; accepted 19 March 2025; published 18 April 2025)

The x-ray excited optical luminescence (XEOL) for defect and near band edge (NBE) transitions combined with simultaneous x-ray absorption measurements are experimentally and theoretically studied on single crystalline ZnO and GaN across the Zn and Ga *K* edges, respectively, in a wide range of sample thicknesses. Increasing the sample thickness leads to the appearance of an inverted line shape and negative edge jump for the XEOL defect response, whereas the line shape of the XEOL NBE edge remains positive. A one-dimensional transport model is developed, which includes experimental geometry, the creation of x-ray generated excitations, diffusion and recombination of the carriers, and reabsorption of x-ray fluorescence and XEOL photons. The model calculations reproduce the experimentally observed changes of the edge shape in the XEOL spectra caused by variation of the sample thickness and reveal surface recombination and optical absorption as the main factors determining the XEOL edge shape for a given sample thickness.

DOI: 10.1103/PhysRevResearch.7.023066

I. INTRODUCTION

X-ray excited optical luminescence (XEOL) spectroscopy is often chosen to investigate the electronic and optical properties of numerous materials by means of a synchrotron radiation source [1–6]. Through a combination of different x-ray absorption spectroscopy (XAS) techniques with XEOL spectroscopy, a useful connection between structural, chemical, and optical material properties can be explored [2,3,6]. XEOL has also gained attention due to its potential application for soft x-ray XAS measurements of thin films grown on luminescent substrates [7,8] and site-selective studies of the optically active atoms giving rise to particular luminescence transitions [9–11]. At the same time, there is a concern with respect to the site selectivity of the XEOL method due to an electronic energy transfer process from an absorbing atom to the neighboring atoms contributing to the measured luminescence response [12]. Therefore, it is highly crucial to compare XEOL with a well-established traditional XAS characterization when searching for site-selective information in the XEOL measurement [13].

One of the interesting characteristic features when comparing the XEOL with XAS is that the luminescence signal may exhibit a negative edge jump in the x-ray absorption near-edge structure (XANES) region, which has been recognized in the first measurement on CaF_2 [14]. The origin of the negative edge jump is controversial and several mechanisms have been proposed [5,14,15]. Bianconi *et al.* [14] explained the negative edge jump with the onset of competing radiative recombination of the 1*s* hole above the *K* edge, based on the anticorrelation behavior between the XEOL and the XAS detected in the x-ray fluorescence mode. It was also proposed that the negative edge jump originates from the ratio of the optical luminescence induced by the *L*-shell and *K*-shell excitations as well as sample thickness [15]. Rogalev and Goulon [5] proposed that the appearance of the negative edge jump of the excitonic XEOL can be associated with a strong surface recombination of a thick sample. However, the recent experimental papers show no negative edge jump for the excitonic XEOL on thick ZnO and GaN samples, but observe a decrease of the XEOL intensity for the defect transitions on ZnO or even a clear negative edge step with the inverted fine-structure features on GaN in the XANES [16–18]. Thus, the existing model must be revised to be consistent with the behavior of the different luminescence transitions.

Here we present a systematic study of the thickness dependence of the XEOL for the defect and near band edge transitions, excited with x-ray energies across the Zn and Ga *K* edges at 10 K, on single crystalline ZnO and GaN samples, respectively. The aim of this study is to obtain a better understanding of the mechanism causing the thickness-induced changes of the XEOL spectra in the XANES region. We propose a method for the calculation of the XEOL spectra from the simultaneously measured XAS based on the analytical solution of the one-dimensional continuity equation for the x-ray excited carriers in the steady-state mode for the low injection regime. We analyze the dependence of the edge shape of the calculated XEOL spectra on the sample thickness, the ratio of surface to bulk recombination rates, and the self-absorption of the emitted optical photons. A very good agreement between

*Contact author: sergiu.levcenco@desy.de

TABLE I. The main characteristics of the *c*-ZnO, *c*-GaN, and *a*-GaN samples.

				Peak position at $E_K + 50$ eV	
Sample	Growth	Substrate	Thickness (μm)	Defect band (eV)	Exciton line (eV)
c-ZnO thin film 1	PLD	*c*-Al_2O_3	1.0 ± 0.1		3.358
c-ZnO thin film 2	PLD	*c*-Al_2O_3	2.0 ± 0.1		3.361
c-ZnO bulk wafer 1	Hydrothermal		54 ± 5	2.1	3.361
c-ZnO bulk wafer 2	Hydrothermal		82 ± 5	2.0	3.361
c-ZnO bulk wafer 3	Hydrothermal		110 ± 5	2.0	3.361
c-ZnO bulk wafer 4	Hydrothermal		188 ± 5	2.0	3.361
c-ZnO bulk wafer 5	Hydrothermal		251 ± 5	2.1	3.361
c-ZnO bulk wafer 6	Hydrothermal		500 ± 5	2.2	3.361
c-GaN thin film	MOCVD	*c*-Al_2O_3	4.0 ± 0.1	2.2	3.486
c-GaN bulk wafer	HVPE		402 ± 5	2.2	3.471
a-GaN thin film	MOCVD	*r*-Al_2O_3	2.7 ± 0.1	2.2	3.428
a-GaN bulk wafer	HVPE		485 ± 5	2.3	3.473

our calculation and the experimental XEOL results is achieved for both defect and near band edge transitions in a wide range of sample thicknesses.

II. EXPERIMENTAL DETAILS

The spectrally resolved XEOL measurements were performed at 10 K with a liquid-He flow cryostat and a 0.5-m Czerny-Turner spectrometer equipped with a thermoelectrically cooled Si charge-coupled device (CCD). A more detailed description of the XEOL setup is published elsewhere [19]. Simultaneous XAS and XEOL measurements were made in a stepwise mode from 200 eV below to 700 eV above the edge of interest (Zn or Ga *K* edges) using a Si(111) monochromator at beamline P65 of PETRA III [20]. The XAS signal was recorded in the fluorescence mode using a Si drift detector. In these simultaneous measurements, the angle of incidence was 45° to the sample surface for most of the samples, while the fluorescence detector was at 90° and the XEOL collection was at 40° to the incident x-ray beam.

Undoped *c*-plane ZnO (*c*-ZnO) single crystalline bulk wafers with varied thickness were grown by a hydrothermal method at Crystec and SurfaceNet. Thin film *c*-ZnO single crystalline samples were deposited by pulsed laser deposition (PLD) on a *c*-plane sapphire substrate [21]. Single crystalline freestanding *c*-plane GaN (*c*-GaN) and *a*-plane GaN (*a*-GaN) samples were grown by hydride vapor phase epitaxy (HVPE) at Kyma Technologies, whereas *c*-GaN and *a*-GaN thin film samples were deposited by metal organic chemical vapor deposition (MOCVD) on *c*- and *r*-plane sapphire substrates at ams-OSRAM International GmbH, Regensburg and Otto-von-Guericke-Universität Magdeburg, Germany, respectively. The thickness of the bulk samples is measured with a dial indicator device. Table I compiles the information on the samples and their luminescence properties obtained from the spectrally resolved XEOL characterization at 10 K.

III. RESULTS

A. ZnO

Figure 1(a) shows the spectrally resolved XEOL of *c*-ZnO single crystal wafers with varied thickness in the region of the broad orange line (OL) defect band centered at ~2.0 eV [22,23] for the x-ray excitation at energies 50 eV below and 50 eV above the Zn *K* edge ($E_K = 9659$ eV) at 10 K. The XEOL intensity is normalized to the intensity of the x-ray flux (I_0) measured with a gas ionization chamber. The XEOL results of the additional *c*-ZnO samples with $d = 110$, 188, and 251 μm are similar to those of 500 μm and are shown in Fig. S1 of the Supplemental Material [24]. We also note that no signal of the OL defect band could be detected on the *c*-ZnO thin films with $d = 1$ and 2 μm. Except for the thinnest bulk sample ($d = 54$ μm), all other bulk samples exhibit similar behavior: a decrease in XEOL intensity with increasing x-ray energy. This result agrees with that on the defect band at ~2.0 eV of a *c*-ZnO thick wafer ($d = 500$ μm) reported by Lin *et al.* [16]. In addition, for *c*-ZnO samples with $d = 500$, 251, and 54 μm, a peak shift of 50–60 meV to higher energy is found, while the other samples show a weak shift or unchanged position [see Fig. 1(a) and Fig. S1 of the Supplemental Material [24]]. The observed blueshift is probably related to the characteristic property of the OL band, namely, a blueshift with increasing excitation power [22,23], or to an in-depth inhomogeneity of the defects involved in the radiative recombination. A higher excitation power in the sample volume is expected for the x-ray energy above the Zn *K* edge as the x-ray attenuation length is significantly shortened.

We also detect strong narrow emission lines at 1.759 and 1.742 eV and weaker lines at 1.745, 1.730, 1.714, 1.708, 1.695, 1.693, and 1.678 eV as well as weak lines at 1.938 and 1.88 eV superimposed on the low-energy side of the OL band in the *c*-ZnO samples [Fig. 1(a) and Fig. S1 of the Supplemental Material [24]]. The lines at 1.938 and 1.88 eV are attributed to artifact signals as these emission lines are also present when the x-ray beam excites the sample holder (see Fig. S2 of the Supplemental Material [24]) or the GaN samples [Fig. 3(a)]. In contrast, a group of lines in the range 1.67–1.76 eV are located in the spectral range of Fe^{3+} luminescence in ZnO [25,26], though the zero phonon line at 1.787 eV is not observed for our samples. It is assumed that this may be connected to the mixed polarization geometry [25] and relatively high Fe concentration effects [26], causing a decrease in intensity of the line at 1.787 eV.

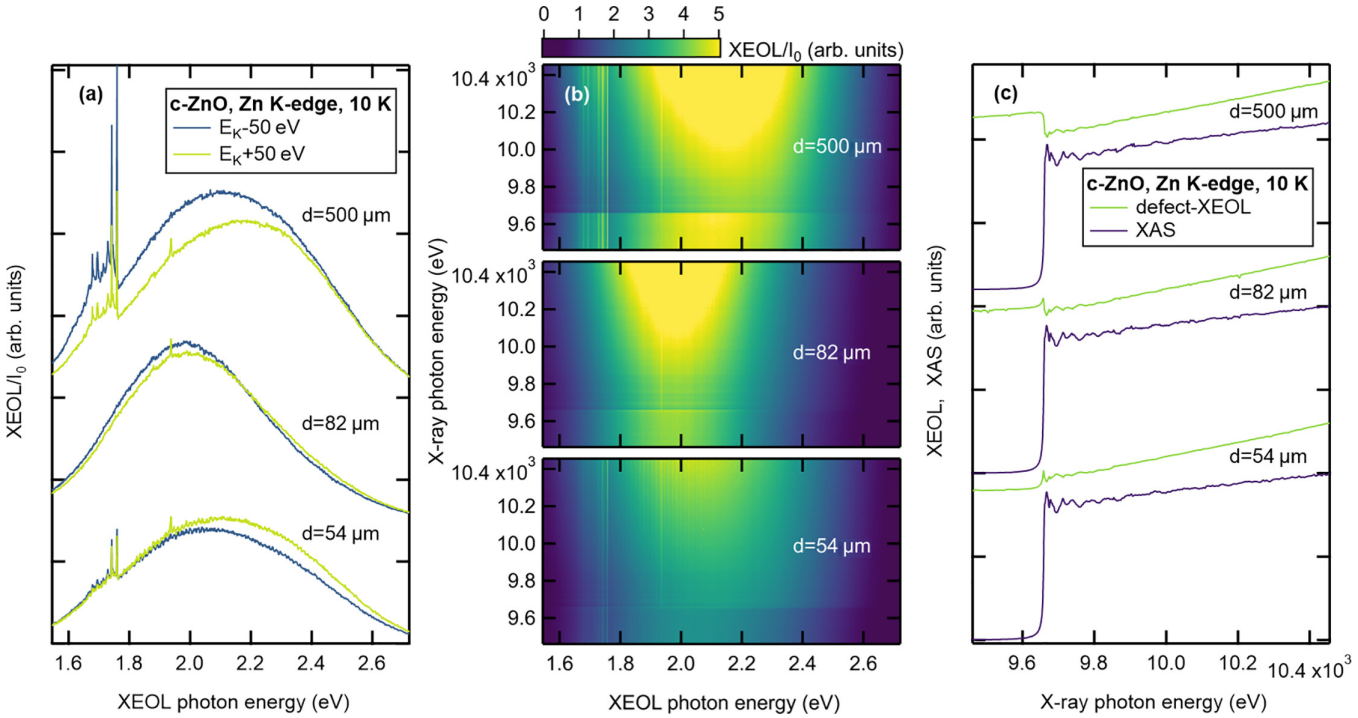

FIG. 1. (a) Normalized defect XEOL at x-ray energy below ($E_K - 50$ eV) and above ($E_K + 50$ eV) the Zn K edge ($E_K = 9659$ eV); (b) 2D defect XEOL mapping across the Zn K edge; and (c) comparison of the defect XEOL intensity and fluorescence XAS measured simultaneously as a function of the x-ray energy at 10 K for c-ZnO single crystals with varied thickness of $d = 500$, 82, and 54 μm. Note that spectra in (a) and (c) for different samples are vertically shifted for more clarity.

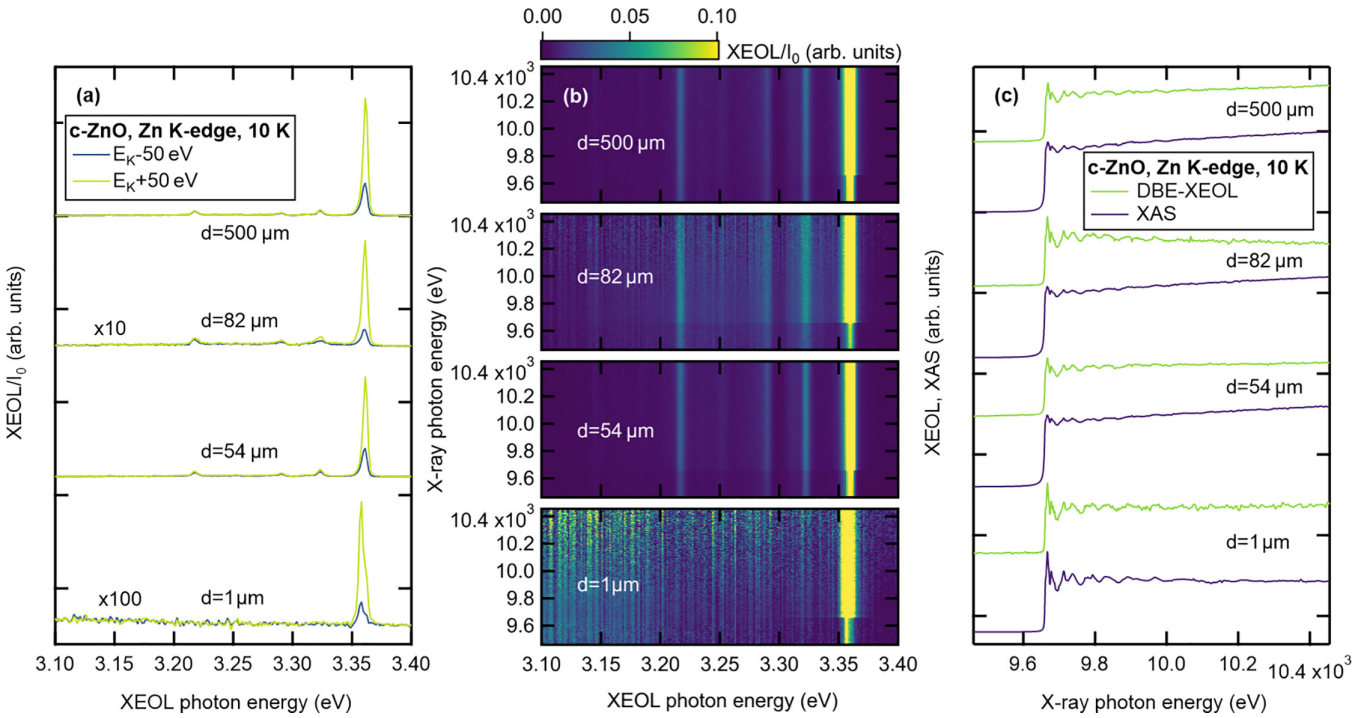

FIG. 2. (a) Normalized NBE XEOL at x-ray energy below ($E_K - 50$ eV) and above ($E_K + 50$ eV) the Zn K edge ($E_K = 9659$ eV); (b) 2D NBE XEOL mapping across the Zn K edge; and (c) comparison of the DBE XEOL intensity and fluorescence XAS measured simultaneously as a function of the x-ray energy at 10 K for c-ZnO single crystals with varied thickness of $d = 500$, 82, 54, and 1 μm. Note that the spectra in (a) and (c) for different samples are vertically shifted for more clarity.

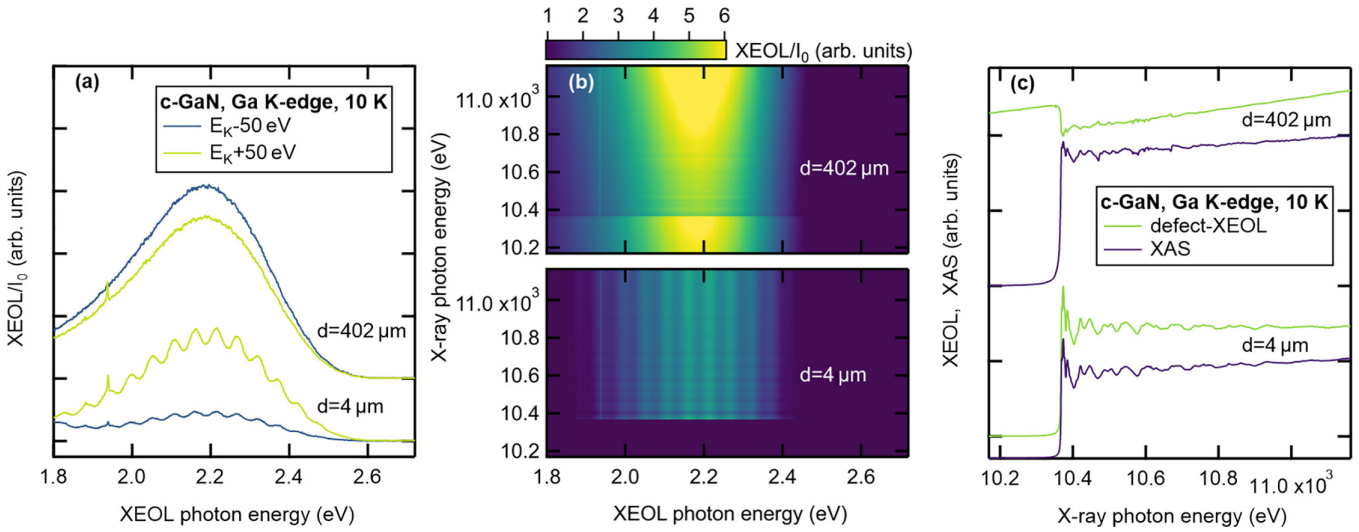

FIG. 3. (a) Normalized defect XEOL at x-ray energy below ($E_K - 50$ eV) and above ($E_K + 50$ eV) the Ga K edge ($E_K = 10\,367$ eV); (b) 2D defect XEOL mapping across the Ga K edge; and (c) comparison of the defect XEOL intensity and fluorescence XAS measured simultaneously as a function of the x-ray energy at 10 K for c-GaN single crystals with different thickness of $d = 402$ and 4 μm. Note that the spectra in (a) and (c) for different samples are vertically shifted for more clarity.

Figure 1(b) shows two-dimensional (2D) XEOL data for the OL defect transition on c-ZnO single crystal wafers measured as a function of x-ray energy across the Zn K edge, demonstrating that the normalized intensity of the OL defect band increases with increasing x-ray energy above the Zn K edge. A closer look at the 2D XEOL data also reveals rapid changes in the XEOL intensity at the Zn K-edge energy E_K especially for samples with $d = 500$ and 82 μm. To analyze this behavior of the OL defect band intensity in more detail, we integrate its intensity in the photon energy range from 1.80 to 2.65 eV to exclude a possible influence from the narrow lines below 1.8 eV. Figure 1(c) presents a comparison of the defect XEOL spectra as a function of x-ray energy and the simultaneously measured fluorescence XAS spectra for the ZnO samples. There is a clear change of the edge shape in the XEOL spectra from negative ($d = 500$ μm) to positive ($d = 54$ μm) but still with an inverted white line and fine-structure intensities relative to those of the XAS spectra. It can also be seen that the edge and the fine structure are more attenuated in the XEOL spectra compared to those of the XAS spectra.

We have also explored the near band edge (NBE) XEOL of the c-ZnO samples. Figure 2(a) displays the NBE XEOL for the c-ZnO bulk wafers ($d = 500$, 82, and 54 μm) and a thin film ($d = 1$ μm). The strongest emission at 3.36 eV, attributed to the exciton bound to a neutral donor (DBE) [27–29], strongly increases in intensity with increasing x-ray energy at the Zn K edge. Note that the thin film with $d = 2$ μm and the other bulk samples ($d = 251$, 188, and 110 μm) give similar results (shown in Figs. S3 and S4 of the Supplemental Material [24]), which are consistent with the earlier XEOL work on the NBE emission for the c-ZnO thick wafer [16]. The 2D XEOL data for the NBE emission is shown in Fig. 2(b). A clear enhancement of the DBE transition is observed above the Zn K edge. A comparison of the simultaneously measured XAS and the XEOL for the DBE intensity integrated over the photon energy range from 3.35 to 3.37 eV is displayed in Fig. 2(c). A positive edge shape of the XEOL is found for all c-ZnO samples regardless of their thicknesses, and the white line and fine structure observed in the XEOL spectra resemble those of the XAS spectra except being even more pronounced in the case of the bulk samples. The observed DBE behavior is significantly different than that of the OL defect band for the same samples (Fig. 1), indicating that the XEOL intensity as a function of x-ray energy depends not only on the sample thickness, but also on the type of emission channel used to monitor the XEOL signal.

B. GaN

Figure 3(a) compares the spectrally resolved XEOL of a c-GaN single crystal wafer ($d = 402$ μm) and a c-GaN thin film ($d = 4$ μm) grown on $c - Al_2O_3$ substrate in the spectral region of the yellow defect (YL1) band at 2.2 eV [30,31] for the x-ray excitation at energies 50 eV below and 50 eV above the Ga K edge ($E_K = 10\,367$ eV) at 10 K. We note that the small oscillations superimposed on the YL1 band of the thin film are due to interference effects [30], while a weak line identified at 1.938 eV is an artifact signal as discussed above for ZnO (see Figs. S2 and S5). We also detect the strong Cr^{3+} emission line of the $c - Al_2O_3$ substrate at 1.79 eV (Fig. S5 of the Supplemental Material [24]), which restricts the spectral range for the thin film sample due to saturation of the CCD detector. As the x-ray excitation energy increases from below to above the edge, the XEOL intensity of the YL1 band decreases for the thick bulk sample, but it increases for the thin film sample. Figure 3(b) shows the 2D XEOL spectra for the YL1 defect band on the c-GaN samples. It can be seen that a drop in XEOL intensity occurs for the thick bulk sample above the Ga K-edge energy E_K. At the same time, the XEOL intensity of the thin film sample is enhanced above E_K. Figure 3(c) displays simultaneously measured XAS and XEOL for the YL1 band, the intensity of which is integrated in the photon energy range from 1.95 to 2.60 eV to exclude an

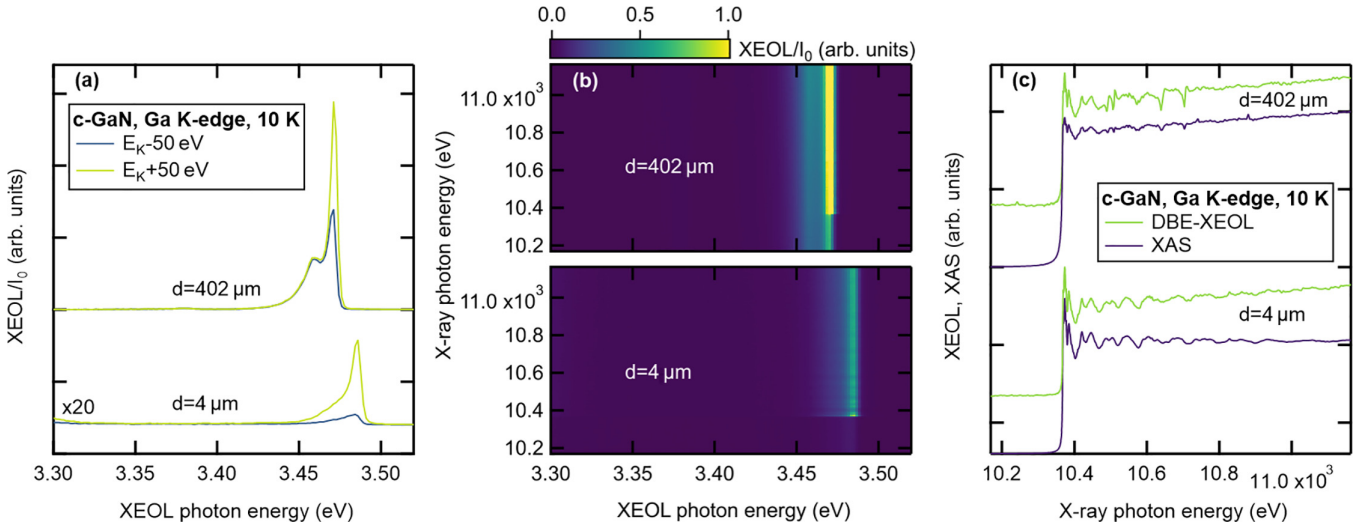

FIG. 4. (a) Normalized NBE XEOL at x-ray energy below ($E_K - 50$ eV) and above ($E_K + 50$ eV) the Ga K edge ($E_K = 10\,367$ eV); (b) 2D NBE XEOL mapping across the Ga K edge; and (c) comparison of the DBE XEOL intensity and fluorescence XAS measured simultaneously as a function of the x-ray energy at 10 K for c-GaN single crystals with different thickness of $d = 402$ and 4 µm. Note that the spectra in (a) and (c) for different samples are vertically shifted for more clarity.

influence of the artifact signal at 1.938 eV. A negative edge and inverted white line and fine structure are found in the XEOL spectrum for the thick bulk sample. In contrast, the XEOL spectrum of the thin film resembles the edge shape and fine structure of the XAS spectrum.

Figure 4(a) shows the spectrally resolved XEOL of the c-GaN samples in the NBE region for the x-ray excitation at energies 50 eV below and 50 eV above the Ga K edge at 10 K. The XEOL spectrum of the c-GaN single crystal bulk wafer is dominated by the DBE transition at 3.471 eV and a two-electron satellite (TES) of the DBE emission at 3.460 eV [30–32]. We observe a similar DBE transition and a less resolved TES in the c-GaN thin film, but their transition energies are blueshifted by about 15 meV due to strain effects, causing a widening of the band gap in the GaN thin layer grown on the sapphire substrate [30,32]. With increasing x-ray excitation energy, the intensity of the DBE emission increases, which is especially noticeable on the 2D XEOL spectra shown in Fig. 4(b). The intensity of the DBE transition (integrated over a photon energy range from 3.46 to 3.48 eV and from 3.44 to 3.49 eV for bulk and thin samples, respectively) and the simultaneously measured XAS are shown in Fig. 4(c) as a function of the x-ray energy. Note that for the c-GaN single crystal bulk wafer we have subtracted the intensity of the TES transition from the integrated intensity of the DBE transition. A positive XEOL edge is observed for both c-GaN samples and the XEOL spectrum is more pronounced relative to the XAS one for the c-GaN single crystal bulk wafer [Fig. 4(c)].

We have additionally investigated the thickness effect on an a-GaN single crystal bulk wafer ($d = 485$ µm) and an a-GaN thin film ($d = 2.7$ µm) in the defect spectral region (Fig. S6 of the Supplemental Material [24]) and in the NBE region (Fig. S7 of the Supplemental Material [24]). The spectrally resolved defect XEOL for the thick bulk sample is dominated not only by the YL1 band but also by the red emission (RL1) band [30]. Nevertheless, we have found a similar behavior of these defect bands to that of the YL1 band of the c-GaN thick bulk sample: a negative edge and an inverted white line and fine structure in the XEOL spectrum. The result of a positive XEOL edge for the a-GaN thick and thin samples in the NBE spectral region also agrees with our findings on the c-GaN samples, indicating a strong role of sample thickness and type of recombination channel used to record the XEOL intensity as a function of the x-ray excitation energy.

IV. DISCUSSION

A. Self-absorption effects in XAS and XEOL

It is generally accepted that due to self-absorption (SA) effects the sample thickness plays a major role in the distortion of the XAS spectrum measured from bulk samples using the x-ray fluorescence (XRF) detection mode [33–36] or the XEOL technique [5]. For this reason, we will first consider SA effects together with our experimental geometry in the interpretation of our XAS and XEOL experimental results.

For a sample of thickness d, the dependence of the XRF-detected XAS intensity I_{XAS} on the x-ray energy E_x is given by the well-known expression [33–36]

$$I_{\mathrm{XAS}}(E_x) = I_0 \frac{\Omega}{4\pi} \frac{\epsilon_f \mu_X}{\mu_{\mathrm{tot}} + \mu_f \frac{\sin\theta_{\mathrm{INC}}}{\sin\theta_{\mathrm{XAS}}}} \times [1 - e^{-(\mu_{\mathrm{tot}}/sin\theta_{INC} + \mu_f/sin\theta_{XAS})d}], \quad (1)$$

where $I_0 = I_0(E_x)$ is the incoming x-ray photon flux measured simultaneously with $I_{\mathrm{XAS}}(E_x)$, Ω is the solid angle centered around the angle θ_{XAS}, at which the XRF is detected [see Fig. 5(a)], θ_{INC} is the angle of incidence of the incoming x-ray beam, ϵ_f is the XRF yield, $\mu_X = \mu_X(E_x)$ is the x-ray absorption coefficient due to core-hole creation at the edge of interest of the element, $\mu_{\mathrm{tot}} = \mu_{\mathrm{tot}}(E_x) = \mu_X(E_x) + \mu_{\mathrm{bg}}(E_x)$ is the total x-ray absorption coefficient including a background absorption μ_{bg} due to different edges and elements, and μ_f is the total x-ray absorption corresponding to the XRF photon energy. In the general case, the evaluation of μ_x from

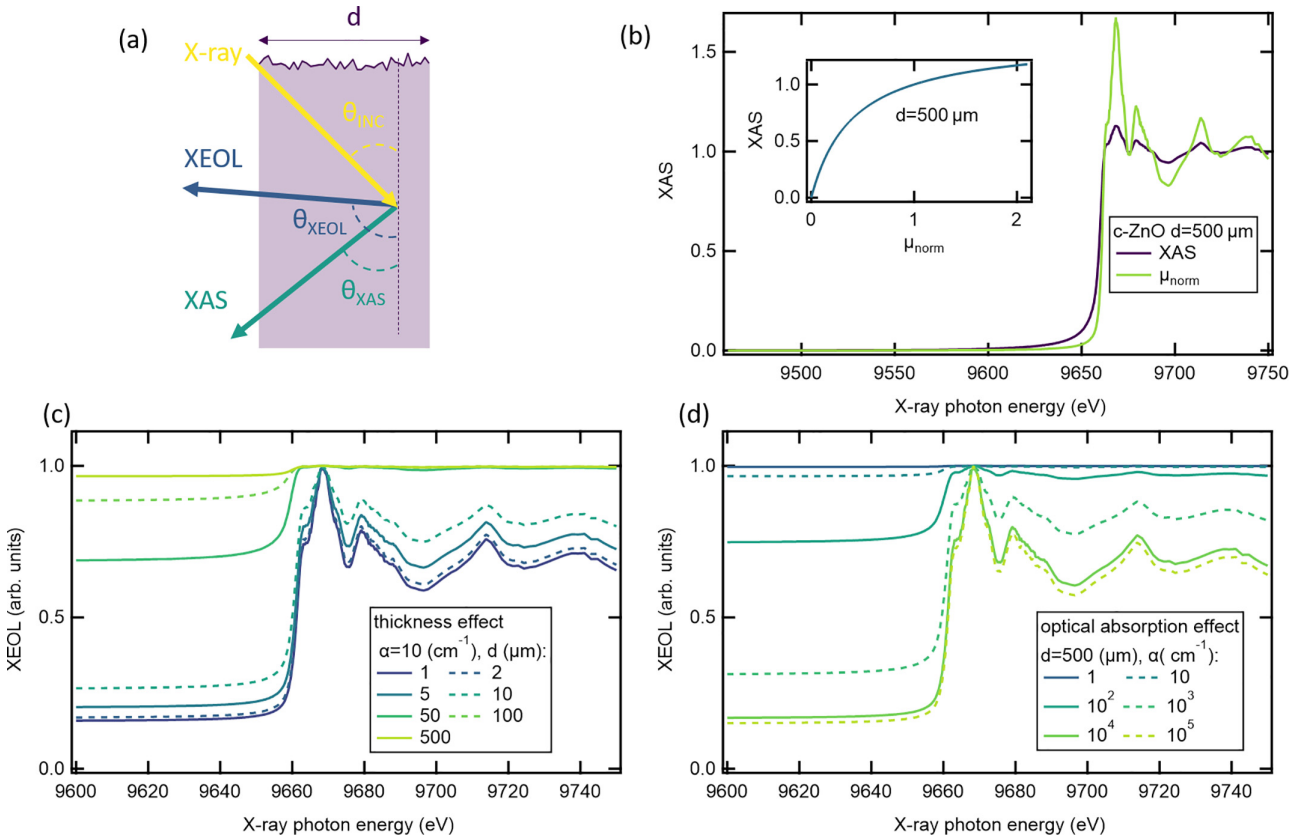

FIG. 5. (a) Schematic diagram illustrating the experimental geometry for the simultaneous XEOL and XAS measurements on a sample with thickness d. (b) Normalized XAS spectrum for the c-ZnO single crystal sample with thickness $d = 500\,\mu$m and the corresponding spectrum corrected for SA effects using the calibration curve shown in the inset. (c) Effect of sample thickness on XEOL spectra normalized to maximum intensity for a fixed absorption coefficient α of 10 cm^{-1} calculated based on Eq. (4). (d) Effect of the optical absorption coefficient on the XEOL spectra normalized to maximum intensity for a fixed sample thickness of $d = 500\,\mu$m calculated based on Eq. (4).

the transcendental equation (1), where $\mu_{\rm tot}$ depends on μ_X, is difficult, and usually impossible for unknown x-ray absorption parameters. For the case of *thick samples*, there are several approaches to obtain μ_X in the XANES [34] and extended x-ray absorption fine-structure (EXAFS) [33,35,36] regions. For the case of *thin samples*, determined by the relation $d \ll (\frac{\mu_{\rm tot}}{\sin\theta_{\rm INC}} + \frac{\mu_f}{\sin\theta_{\rm XAS}})^{-1}$, Eq. (1) simplifies to $I_{\rm XAS}(E_x) = I_0 \frac{\Omega}{4\pi}\epsilon_f \mu_X d/\sin\theta_{\rm INC}$, indicating that μ_X is directly accessible from the XRF-detected XAS measurement under the assumption of an x-ray energy-independent ϵ_f. For an *arbitrary sample thickness*, the approximate solution for μ_X can be numerically calculated by using a few terms of the Taylor series for the exponential term in Eq. (1) [37]. Alternatively, the calibration curve method can be applied, which considers the normalized experimental XAS spectrum, $[I_{\rm XAS}(E_x)/I_0]_{\rm norm}$, and the normalized absorption $\mu_{\rm norm} = \mu_X/(\mu^+_{\rm tot} - \mu_{\rm bg})$, with $\mu^+_{\rm tot} - \mu_{\rm bg}$ being the edge step, $\mu^+_{\rm tot} = \mu_{\rm tot}(E^+_K)$, and E^+_K denoting the energy above the corresponding x-ray edge of interest [38,39]:

$$\left[\frac{I_{\rm XAS}(E_x)}{I_0}\right]_{\rm norm} = C_{\rm norm}\frac{\mu_{\rm norm}(\mu^+_{\rm tot} - \mu_{\rm bg})}{\mu_{\rm tot} + \mu_f \frac{\sin\theta_{\rm INC}}{\sin\theta_{\rm XAS}}} \times [1 - e^{-(\mu_{\rm tot}/sin\theta_{INC} + \mu_f/sin\theta_{XAS})d}]. \quad (2)$$

$C_{\rm norm}$ is the normalization constant determined at E^+_K where $\mu_{\rm norm} = 1$ as [8]

$$C_{\rm norm} = \left[\frac{\mu^+_{\rm tot} - \mu_{\rm bg}}{\mu^+_{\rm tot} + \mu_f \frac{\sin\theta_{\rm INC}}{\sin\theta_{\rm XAS}}}[1 - e^{-(\mu^+_{\rm tot}/sin\theta_{INC} + \mu_f/sin\theta_{XAS})d}]\right]^{-1}. \quad (3)$$

However, instead of trying to calculate $\mu_{\rm norm}$ from $[I_{\rm XAS}(E_x)/I_0]_{\rm norm}$, this method uses Eq. (2) to calculate an array of $\{\mu_{\rm norm}; [\frac{I_{\rm XAS}(E_x)}{I_0}]_{\rm norm}\}$ pairs, the so-called calibration curve, by assuming different values for $\mu_{\rm norm}$ and using tabulated constant values for $\mu_{\rm bg}$, μ_f, and $\mu^+_{\rm tot}$. Subsequently, $\mu_{\rm norm}$ can be determined from the experimental $[\frac{I_{\rm XAS}(E_x)}{I_0}]_{\rm norm}$ spectrum using the calibration curve instead of Eq. (2). The inset of Fig. 5(b) shows the calibration curve for c-ZnO with $d = 500\,\mu$m, the set of x-ray absorption parameters for ZnO given in Table II, and the experimental geometry parameters $\theta_{\rm INC} = 45^\circ$ and $\theta_{\rm XAS} = 45^\circ$. The x-ray absorption parameters are calculated with the HEPHAESTUS software [40] based on the density value of 5.6 g cm^{-3} for ZnO [41] and 6.1 g cm^{-3} for GaN [42]. Figure 5(b) shows the normalized experimental XAS spectrum of c-ZnO with $d = 500\,\mu$m processed with the ATHENA software [40] and the corresponding $\mu_{\rm norm}$ calculated with the calibration curve method. It can be observed that the onset of $\mu_{\rm norm}$ is steeper and shifted to higher x-ray energy

TABLE II. The μ_f, μ_{bg}, and μ_{tot}^+ x-ray absorption coefficient parameters for ZnO and GaN. The density of 5.6 g cm^{-3} for ZnO [41] and 6.1 g cm^{-3} for GaN [42] are used for the parameter calculation with the HEPHAESTUS software [40].

Material	E_K (eV)	$\mu_f(K_{a1})$ (cm^{-1})	$\mu_{bg}(E_K - 50$ eV) (cm^{-1})	$\mu_{tot}^+(E_K + 50$ eV) (cm^{-1})
ZnO	9659	224	168	1136
GaN	10367	220	163	1111

compared to the experimental XAS. Furthermore, the intensity of the white line and the other fine-structure features is significantly higher in μ_{norm}. Both features are known to be the result of the SA effect for measurements of thick samples [33–35]. As there is some uncertainty for the input parameters, including x-ray absorption, geometry, and sample thickness, we have additionally estimated the influence of ±10% variation in each of these parameters on the calculated μ_{norm} for both thin (∼1 μm) and thick (∼110 μm) ZnO samples (see Figs. S8–S11 of the Supplemental Material [24]). It turns out that the sample thickness has the smallest effect on μ_{norm} (<1% relative change) for both types of samples. For the thin sample, all parameter variations induce <1% relative change for μ_{norm}, with the strongest effects from μ_{tot}^+ (∼0.8%) and θ_{INC} (∼0.6%) variation. For the thick sample, however, μ_{tot}^+ variation induces the strongest relative change of 8% for μ_{norm}, while μ_{bg} and μ_f variations cause 4% relative change of μ_{norm}, and θ_{INC} and θ_{XAS} variation introduces only 3% relative change of μ_{norm}. It should be mentioned that the set of x-ray absorption parameters for GaN is similar to that for ZnO (see Table II), indicating that the uncertainties estimated for ZnO are also applicable to the calculation of μ_{norm} for GaN samples.

In a similar way, SA effects can be invoked for the XEOL measurements [5]. We adopt the result of Ref. [5] to our geometry of the incoming x-ray beam and thus the expression for XEOL is given by

$$I_{XEOL}(E_x) = I_0 \frac{\Omega}{4\pi} \frac{q\mu_{tot}}{\mu_{tot} + \alpha \frac{\sin\theta_{INC}}{\sin\theta_{XEOL}}} \times [1 - e^{-(\mu_{tot}/sin\theta_{INC} + \alpha/sin\theta_{XEOL})d}], \quad (4)$$

where q is the XEOL yield, θ_{XEOL} is the angle at which the XEOL is detected [see Fig. 5(a)], and α is the absorption coefficient corresponding to the XEOL emission energy. Moreover, μ_X of Eq. (1) is replaced by μ_{tot} in Eq. (4) to account for the contribution of all the absorbed x-ray photons to the generation of the electron-hole pairs involved in the XEOL emission.

Since we know μ_{norm} from the XAS measurements and the values of μ_{bg} and μ_{tot}^+ (Table II), we can calculate μ_{tot} and thus simulate an XEOL spectrum assuming a constant value for q in Eq. (4). In Fig. 5(c), a series of XEOL spectra normalized to maximum intensity (at a white line maximum for a calculated set of spectra) with varied thickness but fixed optical absorption coefficient is plotted. A pronounced shift of the inflection point to lower energies and a strong reduction of the magnitude of the XEOL fine structure are clearly observed with increasing sample thickness, similar to the SA effects observed for XRF-detected XAS in Fig. 5(b). In addition, we examine the effect of varying the optical absorption coefficient α for the thickest sample with $d = 500$ μm [see Fig. 5(d)]. The higher α is chosen, the closer the XEOL spectrum resembles that from the thinnest sample in Fig. 5(c), implying that a very strong absorption of the emitted photons can compensate the effect of the thickness on the XEOL spectra. This originates from the fact that for strong optical absorption the emitted photons can escape the material only from a small depth below the sample surface and hence the thickness of the sample becomes irrelevant. We also observe a nearly constant XEOL signal for smaller α values [see Fig. 5(d)] as the exponential term in Eq. (4) can be neglected and $\mu_{tot} \approx \mu_{tot} + \alpha \frac{\sin\theta_{INC}}{\sin\theta_{XEOL}}$. Though the observed increase in magnitude of the DBE XEOL fine structure for the thinner c-ZnO (Fig. 2) and $c-$GaN (Fig. 4) samples can be correlated with SA effects, the simulations cannot reproduce the negative defect XEOL edge and inverted fine structure measured on the same samples (Figs. 1 and 3). Thus, we conclude that the conventional approach based only on the experimental geometry and SA effects is insufficient to analyze our thickness-dependent XEOL data. Instead, the creation, diffusion, and nonradiative recombination of the x-ray generated charge carriers must also be taken into account.

B. One-dimensional theoretical model of thickness-dependent XEOL

The number of XEOL photons emitted at a certain depth in the sample depends on the density of excited charge carriers at this depth. However, the depth profile of excess electron-hole pairs generated by absorption of the hard x-ray photons is not only determined by the penetration depth of the x-ray beam into the volume of the crystal. It is also influenced by the diffusion and recombination of the generated carriers. To explore these effects in more detail, we will extend a one-dimensional photoconductivity model [43] by taking into consideration the experimental geometry, the carrier generation by hard x-ray excitation, and the SA effect of the emitted XEOL photons. The incoming x-ray beam forms an angle of incidence θ_{INC} with respect to the sample surface, while the detection of XEOL photons occurs at the angle θ_{XEOL} relative to the sample surface [see Figs. 5(a) and 6(a)]. In the absorption process a single x-ray photon creates $\frac{qE_x}{E_{ee}}$ electron-hole pairs, where q is again the efficiency of the energy transfer (XEOL yield), E_x is the x-ray photon energy, and E_{ee} is the average creation energy for a single electron-hole pair [5]. A continuity equation for the excess carrier concentration ρ is expressed as the sum of the generation, diffusion, and recombination terms [5,43]:

$$\frac{\partial\rho}{\partial t} = I_0 \frac{qE_x}{E_{ee}} \frac{\mu_{tot}}{\sin\theta_{INC}} e^{-\mu_{tot}\, z/sin\theta_{INC}} + D\frac{d^2\rho}{dz^2} - \frac{\rho}{\tau}, \quad (5)$$

where ρ is the excess carrier concentration, I_0 is the incident x-ray photon flux, μ_{tot} is the total x-ray absorption coefficient, z is the spatial coordinate associated with the distance from

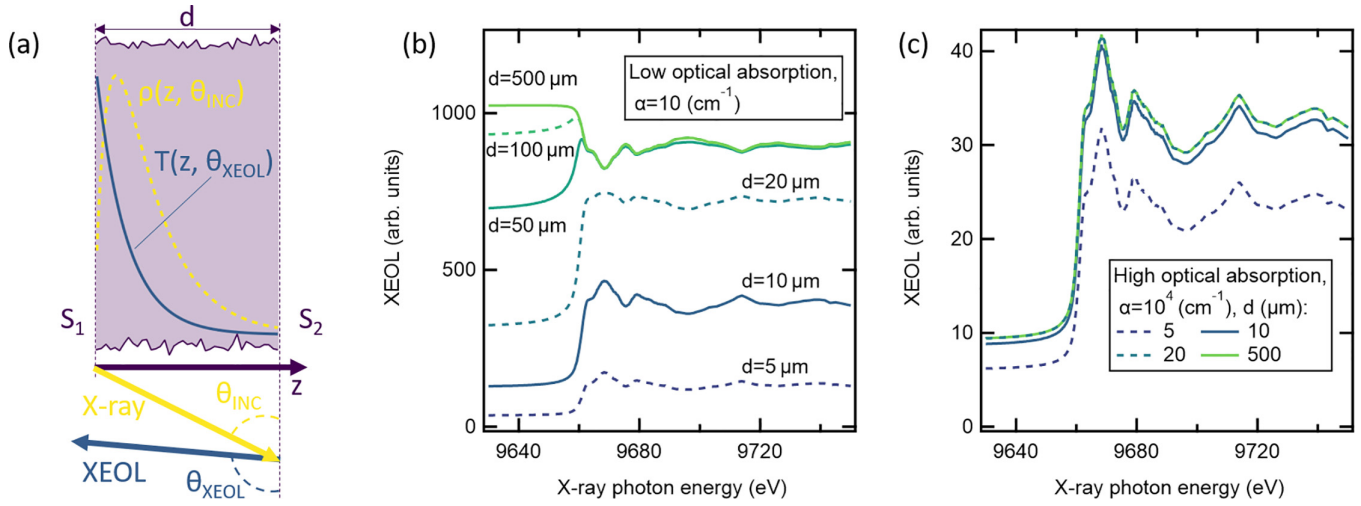

FIG. 6. (a) Schematic diagram illustrating the carrier concentration profile $\rho(z,\ \theta_{\rm INC})$ and the transmission probability of the emitted XEOL photons $T(z,\ \theta_{\rm XEOL})$ for a bulk sample with thickness d and front (S_1) and back (S_2) surface recombination velocities. The XEOL spectra calculated using Eq. (10) for the c-ZnO single crystal samples with varied thickness are plotted for the case of (b) low optical absorption coefficient ($\alpha = 10\ \text{cm}^{-1}$) and (c) high optical absorption coefficient ($\alpha = 10^4\ \text{cm}^{-1}$). The identical set of parameters ($L = 3\,\mu\text{m}$, $\xi_1 = 5$, $\xi_2 = 5$, $\theta_{\rm INC} = 45^\circ$, $\theta_{\rm XEOL} = 95^\circ$) is used in both cases.

the front surface of the sample, D is the diffusion constant, and τ is the total lifetime of the excess carriers and relates to the radiative (τ_R) and nonradiative (τ_{nR}) lifetimes via $\frac{1}{\tau} = \frac{1}{\tau_R} + \frac{1}{\tau_{nR}}$ [44]. For a steady-state condition with $\frac{\partial \rho}{\partial t} = 0$, the general solution of this differential equation [Eq. (5)] can be written as

$$\rho(z) = C_1 e^{-z/L} + C_2 e^{z/L} + C_3 e^{-\mu' z}, \tag{6}$$

where $L = \sqrt{D\tau}$ is the diffusion length, $\mu' = \mu_{\rm tot}/\sin\theta_{\rm INC}$, and $C_3 = I_0 \frac{qE_x}{E_{ee}} \tau \mu' / [1 - (\mu' L)^2]$. Here, the constants C_1 and C_2 are determined by boundary conditions [43], which equate the recombination currents to the surface recombination rates at the front and back sample surfaces:

$$\left| -D\frac{d\rho}{dz} = -\rho S_1 \right|_{z=0}, \tag{7a}$$

$$\left| -D\frac{d\rho}{dz} = \rho S_2 \right|_{z=d}, \tag{7b}$$

where S_1 and S_2 are the front and back surface recombination velocities, respectively [Fig. 6(a)], and d is the sample thickness. This yields the following dimensionless ratios for the constants in Eq. (6):

$$\frac{C_1}{C_3} = \frac{(\xi_1 - 1)(\xi_2 - \mu' L)e^{d(1/L - \mu')} - (\xi_1 + \mu' L)(\xi_2 + 1)e^{2d/L}}{(\xi_1 - 1)(1 - \xi_2) + (\xi_1 + 1)(\xi_2 + 1)e^{2d/L}}, \tag{8a}$$

$$\frac{C_2}{C_3} = \frac{(\xi_1 + \mu' L)(\xi_2 - 1) - (\xi_1 + 1)(\xi_2 - \mu' L)e^{d(1/L - \mu')}}{(\xi_1 - 1)(1 - \xi_2) + (\xi_1 + 1)(\xi_2 + 1)e^{2d/L}}, \tag{8b}$$

where $\xi_1 = S_1 L/D$ and $\xi_2 = S_2 L/D$ are the ratios of surface to bulk recombination rates for the front and back sample surfaces, respectively [43]. Assuming that the luminescence is proportional to the number of excess carriers (low injection condition), we evaluate the measured XEOL intensity $I_{\rm XEOL}$ from the depth-dependent excess carrier density $\rho(z)$ for the minority carriers (holes in n-type and electrons in p-type samples) as [44]

$$I_{\rm XEOL} = \frac{\rho}{\tau_R} = \frac{1}{\tau_R} \int_0^d \rho(z) T(z) dz, \tag{9}$$

where $T(z) = e^{-\alpha z/\sin\theta_{\rm XEOL}}$ represents a Beer's law term for the SA effect with α being the absorption coefficient at the energy corresponding to the emitted XEOL photons. Finally, by inserting Eq. (6) into Eq. (9) and by integrating over the thickness d of the sample, we derive the general expression for the detected XEOL intensity:

$$I_{\rm XEOL} = I_0 \frac{qE_x}{E_{ee}} \frac{\tau}{\tau_R} \frac{\mu'}{1 - (\mu' L)^2} \left[\frac{C_1}{C_3} \frac{1 - e^{-d(1/L + \alpha')}}{1/L + \alpha'} + \frac{C_2}{C_3} \frac{e^{d(1/L - \alpha')} - 1}{1/L - \alpha'} + \frac{1 - e^{-d(\mu' + \alpha')}}{\mu' + \alpha'} \right], \tag{10}$$

where $\alpha' = \alpha/\sin\theta_{\rm XEOL}$ and the dimensionless ratios $\frac{C_1}{C_3}$ and $\frac{C_2}{C_3}$ are functions of material parameters as defined above in Eqs. (8a) and (8b). On the basis of this general result, we consider the effect of the sample thickness on the XEOL

intensity when the x-ray energy is tuned across the edge for the two extreme situations of thin and thick sample limits. In particular, we address the question of whether a negative or a positive edge shape of the XEOL spectrum results for the different scenarios.

For the *thin sample limit*, it suffices to use the first two terms of the Taylor series for the exponential functions ($e^x \approx 1 + x$) in Eqs. (8) and (10), reducing the general expression to

$$I_{\mathrm{XEOL}} = I_0 \frac{qE_x}{E_{ee}} \frac{\tau}{\tau_R} \frac{d^2}{d(1+\xi_1)(1+\xi_2) + L(\xi_1+\xi_2)} \frac{\mu_{\mathrm{tot}}}{\sin\theta_{\mathrm{INC}}}. \tag{11}$$

The XEOL intensity in the thin sample limit is thus proportional to the total x-ray absorption coefficient μ_{tot} and to the x-ray photon energy E_x, but it is independent of SA effects of the emitted light as long as the following constraints are valid: $d \ll (L^{-1} + \alpha')^{-1}$, $d \ll (|L^{-1} - \alpha'|)^{-1}$, $d \ll (\mu' + \alpha')^{-1}$, $d \ll (|L^{-1} - \mu'|)^{-1}$, and $d \ll L/2$. Because the ratio of I_{XEOL}/E_x resembles the shape of μ_{tot}, a positive edge is expected in the XEOL spectrum.

For the *thick sample limit* with $d \gg 1/\mu'$ and $d \gg L$, the exponential functions with a negative exponent and the term $\frac{C_2}{C_3}(e^{d(1/L-\alpha')} - 1)$ can be neglected in Eq. (10) and it can be simplified to

$$I_{\mathrm{XEOL}} = I_0 \frac{qE_x}{E_{ee}} \frac{\tau}{\tau_R} \frac{\mu'}{1-(\mu' L)^2} \times \left[-\frac{\xi_1 + \mu' L}{\xi_1 + 1} \frac{1}{1/L + \alpha'} + \frac{1}{\mu' + \alpha'} \right]. \tag{12}$$

The XEOL intensity in the thick sample limit thus has a complex relationship with the parameters ξ_1, μ', L, and α', though it does not depend on the sample thickness. To gain some insight into the interplay of these parameters, it is useful to analyze Eq. (12) for different rates ξ_1 of the front surface to bulk recombination.

For the case of *arbitrary values of* ξ_1, Eq. (12) can be rearranged into

$$I_{\mathrm{XEOL}} = I_0 \frac{qE_x}{E_{ee}} \frac{\tau}{\tau_R} \frac{1}{(\xi_1+1)(1+\alpha' L)} \times \left[\frac{(\mu')^2 L + \mu'(\alpha' L + 1 + \xi_1)}{(\mu')^2 L + \mu'(\alpha' L + 1) + \alpha'} \right]. \tag{13}$$

The rational fraction with polynomials of μ' in Eq. (13) represents a monotonically nondecreasing function of μ' across the x-ray edge if its first derivative with respect to μ' is $\geqslant 0$. In this case, the XEOL spectrum will exhibit a positive edge shape. The condition for the derivative is met for large optical absorption coefficients of the emitted XEOL photons and leads to the following bottom constraint for α in order to observe a positive XEOL edge:

$$\alpha \geqslant \gamma \sin\theta_{\mathrm{XEOL}} \left(\sqrt{1 + \frac{(\mu_{\mathrm{tot}})^2 \xi_1}{\gamma^2 \sin^2\theta_{\mathrm{INC}}}} - 1 \right), \tag{14}$$

where $\gamma = \mu_{\mathrm{tot}}/\sin\theta_{\mathrm{INC}} + 0.5(\xi_1 + 1)/L$. Otherwise, i.e., if α is smaller than this value, the increase of μ_{tot} causes a decrease of I_{XEOL} and hence a change of the XEOL edge shape from positive to negative. The optical absorption coefficient of the emitted XEOL photons is thus a decisive factor for the shape of the measured XEOL spectrum for thick samples.

For very *strong front surface recombination* compared to the bulk one, $\xi_1 \to \infty$ and Eq. (13) reduces to

$$I_{\mathrm{XEOL}} = I_0 \frac{qE_x}{E_{ee}} \frac{\tau}{\tau_R} \frac{1}{(1+\alpha' L)} \frac{\mu'}{(1+\mu' L)(\mu' + \alpha')}. \tag{15}$$

In this case, the shape of the edge in the XEOL spectrum strongly depends on the actual values of the diffusion length, the absorption coefficient for the emitted XEOL photons, and the geometrical angles. For high values of α, when the relation $\alpha > (\mu_{\mathrm{tot}}/\sin\theta_{\mathrm{INC}})^2 L \sin\theta_{\mathrm{XEOL}}$ is satisfied for all values of μ_{tot} across the x-ray edge, the XEOL spectrum will exhibit a positive edge. As soon as this constraint becomes invalid, a further increase in μ_{tot} will correspond to a decrease in I_{XEOL} and thus result in a distortion of the edge in the XEOL spectrum. In contrast, for very low values of α, the XEOL intensity inversely depends on μ_{tot} as $I_{\mathrm{XEOL}} \propto (1 + \mu_{\mathrm{tot}} L/\sin\theta_{\mathrm{INC}})^{-1}$, thereby predicting a negative XEOL edge with a magnitude proportional to the $L/\sin\theta_{\mathrm{INC}}$ term. We also note that for $\alpha' \to 0$, $\theta_{\mathrm{INC}} \to 90^\circ$, and $\tau = \tau_R$, Eq. (15) agrees with the earlier model [5], where infinite surface recombination was assumed but the experimental geometry and SA effects were not included.

For the case of a very *small ratio of the front surface to bulk recombination*, $\xi_1 \to 0$ and Eq. (13) represents a monotonically nondecreasing function of μ' across the x-ray edge as $\alpha' \geqslant 0$. The XEOL edge shape is thus always positive in this case; however, the magnitude of the edge decreases with decreasing α'. In the most extreme case, when the SA effect is completely absent ($\alpha' = 0$), the XEOL intensity in the thick sample limit becomes independent of μ' and has just a linear dependence on E_x.

To complete the case of thick samples, it is useful to discuss the effect of *strong SA of the XEOL photons*. For samples with intermediate thickness ($d \gg L/2$) but high values of α ($\alpha' \gg 1/d$), the general expression for the XEOL intensity is also reduced to Eqs. (12) and (13). The model further predicts a positive edge in the XEOL independently of ξ_1 provided the corresponding constraint on α is fulfilled [Eq. (14)]. For direct semiconductors the typical values of α in the NBE region can be an order of magnitude larger than the values of μ_{tot} at the K edge. With increasing sample thickness, the condition $d \gg (\alpha/\sin\theta_{\mathrm{XEOL}})^{-1}$ is thus met long before $d \gg (\mu_{\mathrm{tot}}/\sin\theta_{\mathrm{INC}})^{-1}$ is fulfilled (except for the very special geometrical configuration of the very small incidence angle θ_{INC} compared to θ_{XEOL}). In other words, the applicability of the thick sample limit is now a consequence of the strong absorption of the XEOL photons, not of the x-ray photons. Therefore, it is very important to account for SA effects in the interpretation of the XEOL data measured on thick samples.

To illustrate the effect of sample thickness over a larger thickness range, we calculate the XEOL spectra using Eq. (10) for either low ($\alpha \sim 10\ \mathrm{cm}^{-1}$) or high ($\alpha \sim 10^4\ \mathrm{cm}^{-1}$) absorption coefficients of the emitted XEOL photons. For both cases, we use the same set of material parameters: $L = 3\,\mu\mathrm{m}$, $\xi_1 = 5$, $\xi_2 = 5$, $\theta_{\mathrm{INC}} = 45^\circ$, and $\theta_{\mathrm{XEOL}} = 95^\circ$. As input for μ_{tot}, we employ an XAS spectrum of ZnO ($d = 500\,\mu\mathrm{m}$) corrected for SA effects and scaled to match the absorption

below the edge to 168 cm^{-1} and above the edge to 1136 cm^{-1} (Table II). For the *low absorption coefficient*, Fig. 6(b) shows how the shape of the XEOL edge changes from a positive edge ($d = 5$, 10, and 20 μm) to a distorted edge (yet still with the initial onset) and an inverted white line and fine structure ($d = 50$ and 100 μm), and finally to a completely negative edge with an inverted fine structure ($d = 500\,\mu m$). The close similarity of the XEOL spectra above 9660 eV for $d > 50$ μm is the result of the thick sample limit scenario [Eqs. (12) and (13)]. Moreover, increasing the sample thickness sample from $d = 50$ to 100 μm enlarges the region of similarity to lower x-ray energies, where μ_{tot} has lower values, until the relation $d \gg (\mu_{tot}/\sin\theta_{INC})^{-1}$ is broken. Note that the selected value of $\alpha \sim 10\,cm^{-1}$ is smaller than the bottom constraint of $\sim 12\,cm^{-1}$ calculated with Eq. (14) and using the value of μ_{tot} below the edge, implying a completely negative XEOL edge for the thick sample. In contrast, for the *high absorption coefficient*, Fig. 6(c) shows that there is no distortion of the XEOL edge, only an increase of the XEOL intensity, which saturates at $d = 20\,\mu m$. Note that the calculated XEOL spectra for $d = 50$ and 100 μm are identical to those for $d = 500\,\mu m$ and are excluded from Fig. 6(c) for simplicity. This saturation behavior corresponds to the scenario of the thick sample limit [Eqs. (12) and (13)] induced by a strong SA of the XEOL photons as discussed above. The selected value of $\alpha \sim 10^4$ cm^{-1} is much larger than the bottom constraint of $\sim 454\,cm^{-1}$ calculated with Eq. (14) and using the largest μ_{tot} values. Overall, it is thus observed that low optical absorption produces positive and negative XEOL edges depending on the sample thickness, while high optical absorption produces only positive XEOL edges, despite an identical x-ray absorption spectrum and identical values for the experimental geometry and material parameters.

C. Quantitative description of experimental XEOL spectra

We now consider the experimental XEOL spectra as a function of x-ray energy E_x discussed in Sec. III. The measured XEOL intensity normalized to the incident x-ray photon flux, $I_{XEOL}^{expt} = I_{XEOL}/I_0$, for the defect or DBE transitions of ZnO and GaN samples [Figs. 1(c), 2(c), 3(c), and 4(c)] is proportional to the XEOL intensity given by the general expression of the one-dimensional XEOL model [Eq. (10)]:

$$I_{XEOL}^{expt} = C_j^0 I_{XEOL}^{theory}/I_0 = C_j \frac{E_x}{E_{ee}} \frac{\mu'}{1-(\mu' L)^2}\left[\frac{C_1}{C_3}\frac{1-e^{-d(1/L+\alpha')}}{1/L+\alpha'} + \frac{C_2}{C_3}\frac{e^{d(1/L-\alpha')}-1}{1/L-\alpha'} + \frac{1-e^{-d(\mu'+\alpha')}}{\mu'+\alpha'}\right], \quad (16)$$

where C_j^0 is the proportionality factor depending on the optical detection system and the solid angle for the XEOL photon collection and $C_j = C_j^0 q \frac{\tau}{\tau_R}$ is the dimensionless scaling factor. The subscript j refers to either defect or DBE transition. This scaling factor introduces an additional model parameter for the evaluation of the experimental XEOL data for each luminescence transition. It is important to point out that the x-ray absorption coefficient μ_{tot} must be known at each x-ray energy in order to calculate the XEOL intensity based on Eq. (10) or (16). The required μ_{tot} data are accessible from the simultaneous XAS measurements, corrected for SA effects and scaled to the absolute x-ray absorption values below and above the corresponding edge computed with the HEPHAESTUS software [40] (Sec. IV A). The use of simultaneously measured XAS spectra instead of literature data for μ_{tot} eliminates possible concerns regarding the x-ray energy scale calibration for the different datasets, potential differences in the experimental geometry, and sample temperature and sample specific property variations [17,45,46].

We evaluate the experimental XEOL spectra using Eq. (16) and the known values of the geometrical parameters ($\theta_{INC} = 45°$, $\theta_{XAS} = 45°$, and $\theta_{XEOL} = 95°$) and sample thicknesses. Note that for the measurement of *c*-ZnO samples with $d = 54\,\mu m$ and $d = 82\,\mu m$ a slightly different geometrical configuration ($\theta_{INC} = 35°$, $\theta_{XAS} = 55°$, *and* $\theta_{XEOL} = 105°$) is used. Furthermore, a low value of $\alpha_{defect} = 10$ cm^{-1} is assumed for the optical absorption coefficient in the spectral region of the defect transitions [47–49]. Figures 7(a) and 8(a) show the calculated and measured XEOL spectra for the defect transitions as well as the SA-corrected XAS spectra of the *c*-ZnO single crystalline samples with $d = 500$, 251, and 54 μm and the *c*-GaN single crystalline samples with $d = 402$ and 4 μm, respectively. The results for the additional *c*-ZnO and *a*-GaN samples are presented in Figs. S12 and S13 of the Supplemental Material [24]. A very good match of calculated and measured XEOL spectra can be observed in all cases. The corresponding model parameters are listed in Table III. A note of caution is that any possible inhomogeneity of the sample at the micron and submicron scale may account for substantial differences in the absorption coefficient and diffusion length values. This may explain some difference in the model parameter values for the samples produced with different growth method or conditions. To reduce a possible influence of the model parameters on each other, we set ξ_1 and ξ_2 to fixed values in the range 10–100 during the fitting procedure. The diffusion length L and the scaling factor C_{defect} thus remain as the only free parameters. We find that independent of the actual ξ_1 and ξ_2 values, the fitting procedure yields similar results for the diffusion length of 2–3 μm and for the scaling factor of (0.7×10^{-3})–(0.9×10^{-3}) for the *c*-ZnO, *c*-GaN, and *a*-GaN bulk samples but a higher scaling factor of 1.3×10^{-2} for the *c*-GaN and *a*-GaN thin film samples (Table III). Based on these values of the diffusion length, the range for the surface recombination rate (S_1 or S_2) is estimated as $0.3 - 5 \times 10^4$ cm/s assuming a carrier diffusion constant of $1\,cm^2\,s^{-1}$. For the bulk samples, the insensitivity of the fit outcome to the variation of ξ_1 and ξ_2 can be understood based on the discussion of the XEOL model in the thick sample limit (Sec. IV B). If the contribution of the quadratic term in the numerator of Eq. (13) is very small relative to the linear term ($\mu' L \ll \alpha' L + 1 + \xi_1$), the XEOL intensity I_{XEOL}^{theory} will be proportional to $\frac{\alpha' L + 1 + \xi_1}{1+\xi_1}$ or even independent of ξ_1 if $\alpha' L \ll 1$. These relations are well fulfilled for the values considered for ξ_1 and for the typical values of $\mu_{tot} \sim 10^2 - 10^3$ cm^{-1}, $L \sim 2 - 3$ μm, and $\alpha_{defect} \sim 10\,cm^{-1}$. Moreover, Eq. (13) thus reduces to the analytical approximation for the case of very strong surface recombination [Eq. (15)], even though the value of ξ_1 is moderate rather than infinite. Consequently, it is difficult to determine the exact moderate values of ξ_1 with this model from the XEOL measurements on thick samples.

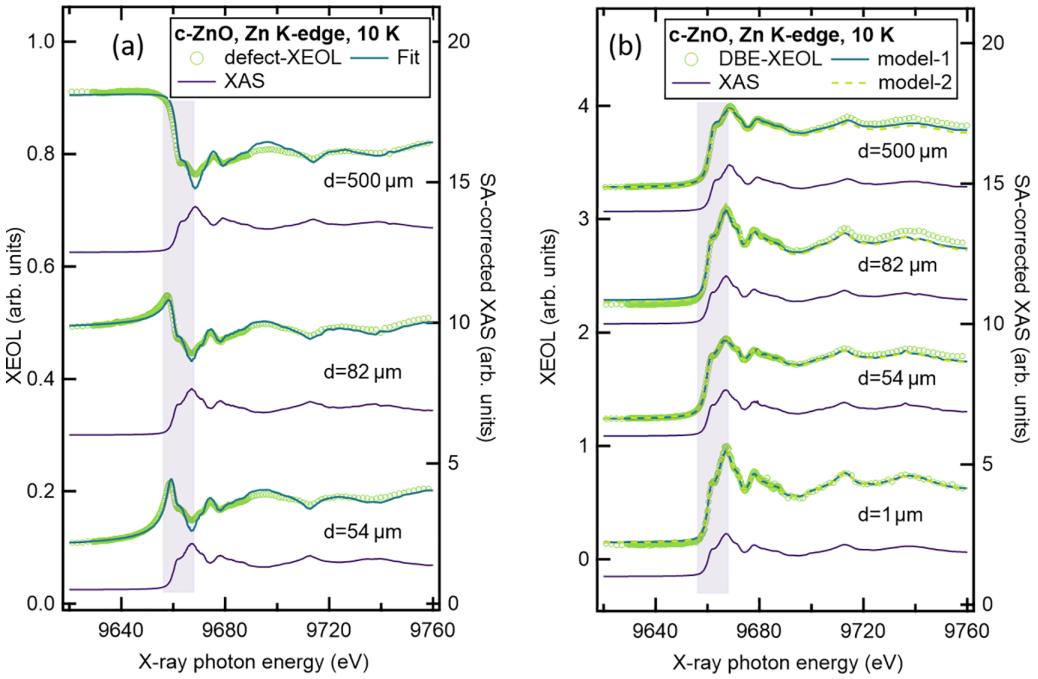

FIG. 7. Calculated (solid line) and measured (circles) XEOL across the Zn *K* edge at 10 K for *c*-ZnO single crystals with varied thickness in the (a) defect and (b) DBE spectral regions. XEOL spectra are calculated using Eq. (16) and the SA-corrected simultaneously measured XAS spectra are also shown (purple solid lines). The highlighted region indicates the Zn *K* edge in the XEOL and XAS spectra. Note that the XEOL and SA-corrected XAS spectra for different samples are vertically shifted for more clarity.

It should be added that for values of ξ_1 and ξ_2 smaller than 10, the fit yields somewhat unreliable results as the L values obtained are then 10 µm or higher, which was not observed in relevant experimental studies on the diffusion length of free carriers in ZnO or GaN [50–52].

In the next step, we evaluate the experimental XEOL spectra for the DBE transitions by using the same geometrical parameters and the ξ_1, ξ_2, and L values obtained from the above analysis of the XEOL spectra for the defect transitions. In this case, there are again two free fit parameters: the optical absorption coefficient α_{NBE} in the spectral region of the DBE transitions and the scaling factor C_{NBE}. We denote this approach as "model 1," emphasizing its assumption that the diffusion length is identical to the one used for the defect transitions and related to the minority carrier diffusion length [as formulated in Eq. (9)]. Figures 7(b) and 8(b) as well as S12(b) and S13(b) of the Supplemental Material [24] show a comparison of the measured and calculated DBE XEOL

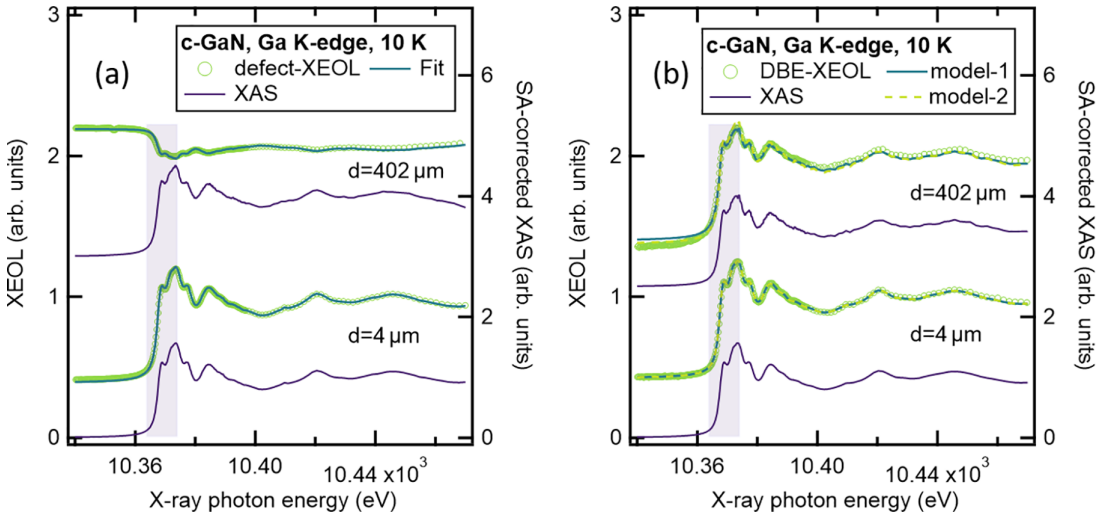

FIG. 8. Calculated (solid line) and measured (circles) XEOL across the Ga *K* edge at 10 K for *c*-GaN single crystals with varied thickness in the (a) defect and (b) DBE spectral regions. XEOL spectra are calculated using Eq. (16) and the SA-corrected simultaneously measured XAS spectra are also shown (purple solid lines). The highlighted region indicates the Ga *K* edge in the XEOL and XAS spectra. Note that the XEOL and SA-corrected XAS spectra for different samples are vertically shifted for more clarity.

TABLE III. Model parameters used in the calculation of the XEOL spectra in the defect region of the *c*-ZnO, *c*-GaN, and *a*-GaN samples.

d (μm)	L (μm)	ξ_1, ξ_2	θ_{INC} (deg)	θ_{XEOL} (deg)	α_{defect} (cm^{-1})	C_{defect}
			c-ZnO			
54	1.8 ± 0.1	10–100	35	105	10	$(0.7 \pm 0.1)\times10^{-3}$
82	1.7 ± 0.1	10–100	35	105	10	$(0.7 \pm 0.1)\times10^{-3}$
110	3.5 ± 0.3	10–100	45	95	10	$(0.9 \pm 0.1)\times10^{-3}$
188	3.2 ± 0.2	10–100	45	95	10	$(0.8 \pm 0.1)\times10^{-3}$
251	2.8 ± 0.2	10–100	45	95	10	$(0.9 \pm 0.1)\times10^{-3}$
500	2.6 ± 0.2	10–100	45	95	10	$(0.8 \pm 0.1)\times10^{-3}$
			c-GaN			
4	2.9 ± 0.2	40–100	45	95	10	$(1.3 \pm 0.1)\times10^{-2}$
402	3.1 ± 0.2	10–100	45	95	10	$(0.8 \pm 0.1)\times10^{-3}$
			a-GaN			
2.7	1.6 ± 0.1	10–100	45	95	10	$(1.3 \pm 0.1)\times10^{-2}$
485	1.7 ± 0.1	10–100	45	95	10	$(0.7 \pm 0.1)\times10^{-3}$

spectra for the *c*-ZnO, *c*-GaN, and a-GaN samples, respectively, and Table IV lists the corresponding model parameters. An excellent agreement between the measured and calculated XEOL spectra is observed in all cases. During the initial fitting with a starting value of 10^3 cm^{-1} for α_{NBE}, it was found that for some samples the fitted value for α_{NBE} reaches 10^5 cm^{-1} or higher, coupled with a fairly large uncertainty for both α_{NBE} and C_{NBE}. To prevent this uncertainty for these samples, the value for α_{NBE} was fixed at 10^5 cm^{-1} during the subsequent fitting (see Table IV). The source of the fitting uncertainty for high α_{NBE} values can also be understood on the basis of the XEOL model for the thick sample limit. When the linear term is significantly larger than the quadratic one ($\mu' L \ll \alpha' L + 1$) in the denominator of Eq. (13), the XEOL intensity is proportional to $\frac{1}{\alpha'}\frac{\mu'}{\mu'(L+1/\alpha')+1}$. Consequently, an increase of the uncertainty in α_{NBE} gives rise to a larger uncertainty in the XEOL intensity and, therefore, in the C_{NBE} value. This analysis also implies that the fit is sensitive to the sum $L + 1/\alpha'$, but not to the individual unknown parameters L or α_{NBE}. Moreover, in the thick sample limit and if $\mu'(L + \frac{1'}{\alpha}) \ll 1$, the XEOL intensity is simply proportional to μ' and neither the determination of α_{NBE} nor of L will be possible from fitting experimental data. Fortunately, the last inequality is not valid for the typical values of μ_{tot} and the estimated values of L and α_{NBE} and, hence, the analysis with model 1 is feasible for the studied samples.

The electronic transport, which may take the form of free charge carriers (uncorrelated electron and hole, as described above) or free excitons (bound electron-hole pairs), is not well studied in our samples. However, previous low-temperature experimental studies have shown that free exciton transport also takes place in ZnO and GaN semiconductors [53,54]. Therefore, we consider a second approach, which associates the diffusion length with the free exciton diffusion length equal to ~0.2 μm for these materials [53,54], but ignores any contribution from the free charge carriers to the formation of the free excitons and as a result to DBE transitions. This approach is denoted as "model 2" and the calculated spectra are shown in Figs. 7(b) and 8(b) as well as Figs. S12(b) and S13(b) of the Supplemental Material [24]. In fact, model 2 yields even better agreement with the measured DBE XEOL spectra than model 1 and it eliminates the fitting uncertainty

TABLE IV. Model parameters used in the calculation of the XEOL spectra in the DBE region of the *c*-ZnO, *c*-GaN and *a*-GaN samples.

	Model 1			Model 2		
d (μm)	L (μm)	α_{NBE} (cm^{-1})	C_{NBE}	L (μm)	α_{NBE} (cm^{-1})	C_{NBE}
			c-ZnO			
1	1.8	1×10^5	3.8 ± 0.1	0.2	1×10^5	0.17 ± 0.01
2	1.8	1×10^5	2.0 ± 0.1	0.2	1×10^5	0.17 ± 0.01
54	1.8	$(2.7 \pm 0.1)\times10^3$	$(4.2 \pm 0.3)\times10^{-3}$	0.2	$(1.5 \pm 0.1)\times10^3$	$(1.7 \pm 0.1)\times10^{-3}$
82	1.7	1×10^5	1.0 ± 0.1	0.2	$(4 \pm 1)\times10^4$	$(4 \pm 1)\times10^{-2}$
110	3.5	1×10^5	2.2 ± 0.1	0.2	$(1.0 \pm 0.1)\times10^4$	$(7.4 \pm 0.3)\times10^{-3}$
188	3.2	1×10^5	2.0 ± 0.1	0.2	$(1.5 \pm 0.1)\times10^4$	$(1.2 \pm 0.1)\times10^{-2}$
251	2.8	$(2.6 \pm 0.1)\times10^3$	$(5.4 \pm 0.3)\times10^{-3}$	0.2	$(1.2 \pm 0.1)\times10^3$	$(1.6 \pm 0.1)\times10^{-3}$
500	2.6	$(2.8 \pm 0.1)\times10^3$	$(5.7 \pm 0.3)\times10^{-3}$	0.2	$(1.3 \pm 0.1)\times10^3$	$(1.6 \pm 0.1)\times10^{-3}$
			c-GaN			
4	2.9	$(4.0 \pm 0.5)\times10^4$	0.5 ± 0.1	0.2	$(6.0 \pm 0.3)\times10^3$	$(0.5 \pm 0.1)\times10^{-2}$
402	3.1	1×10^5	1.9 ± 0.1	0.2	$(1.0 \pm 0.1)\times10^4$	$(0.7 \pm 0.1)\times10^{-2}$
			a-GaN			
2.7	1.6	1×10^5	1.2 ± 0.1	0.2	1×10^5	0.16 ± 0.01
485	1.7	$(0.6 \pm 0.1)\times10^3$	$(1.3 \pm 0.1)\times10^{-3}$	0.2	$(0.4 \pm 0.1)\times10^3$	$(1.0 \pm 0.1)\times10^{-3}$

for α_{NBE} for the bulk samples (Table IV). However, comparisons of all fit results and the dependencies of the XEOL model in the thick sample limit discussed above suggest that determination of the actual value of the diffusion length from experimental XEOL data is rather difficult, especially if α_{NBE} is also unknown. Nevertheless, this model 2 with the exciton electronic transport can be justified for the *c*-ZnO thin film samples, as no defect emission due to recombination of uncorrelated charge carriers can be found.

Rogalev and Goulon developed a somewhat similar one-dimensional model for the excitonic XEOL in ZnO, but without including the optical absorption of the excitonic XEOL photons and the experimental geometry [5]. That model predicts a change from the positive to a negative edge shape for the excitonic XEOL spectra with increasing the sample thickness from 1 μm to hundreds of μm. We have shown experimentally that, contrary to this previous prediction, the edge shape of the DBE XEOL spectra in ZnO is not altered by the sample thickness. Furthermore, we propose a generalized model that properly incorporates SA effects for the emitted XEOL photons and the experimental geometry. It thus provides an accurate description of the thickness-dependent XEOL spectra measured in both the defect and the NBE spectral regions.

To complete our discussion, let us briefly consider possible limitations and additional aspects in the analysis of XEOL data. The generalized one-dimensional model assumes that the XEOL intensity is proportional to the excess carrier density [Eq. (9)]. However, if the material is lightly doped or if the excitation power is very high, then the low injection approximation no longer holds true. In this case dependences of the XEOL intensity and the recombination lifetime on the excitation power [44] should also be considered. In addition, our model ignores a possible deviation from the linear dependence on the excitation power for the excitonic transitions [55]. However, this assumption should be justified since low-temperature photoluminescence measurements on GaN and ZnO imply that the intensity of the DBE transitions varies almost linearly with the excitation power [23,30]. Another important effect to be considered is a built-in surface electric field [56], resulting in a space-charge depletion layer in the surface region of the sample, especially, when the XEOL measurements are carried out with soft x-rays [57]. The model presented above is developed for a homogeneous system (single crystalline samples), but it will also be interesting to explore the treatment of powder samples to understand an additional impact of grain size and light-scattering effects on the XEOL response. Finally, extending the model to more than one dimension can be very helpful when studying semiconductor nanowires [3,58] or individual grains and their boundaries in polycrystalline materials [59,60] by means of XEOL characterization with a submicron spatial resolution.

V. CONCLUSIONS

To summarize, we have performed systematic simultaneous measurements of the XEOL and fluorescence XAS as a function of the sample thickness for *c*-ZnO, *c*-GaN, and *a*-GaN single crystalline bulk and thin film samples at the Zn and Ga *K* edges, respectively. For XEOL, we have investigated the luminescence in both the defect and the near band edge spectral regions. In the XANES region the thickness variation strongly affects the line shape of the defect XEOL but not of the near band edge XEOL. We have developed an analytical one-dimensional XEOL model in the low injection state, which takes into account the generation of the free carriers by the x-ray absorption, carrier diffusion, recombination, experimental geometry, and self-absorption of the XEOL photons. It is found that the proportionality between the XEOL signal and the x-ray absorption coefficient exists only for very thin samples. In contrast, for an arbitrary sample thickness, the line shape of the XEOL differs from the XAS, depending on a number of material parameters including the diffusion length, the ratio of surface to volume recombination, and the absorption coefficient of the emitted XEOL photons as well as the geometrical parameters defining the experiment. Using this model and the x-ray absorption coefficient derived from the simultaneously measured XAS corrected for self-absorption effects, we demonstrate that the thickness-dependent line shape of the XEOL spectra for both defect and near band edge regions can be explained quantitatively very well for the ZnO and GaN samples. This work thus demonstrates that the simultaneous XEOL and XAS measurements can be used as an efficient tool for the accurate interpretation and quantitative analysis of the XEOL spectra.

ACKNOWLEDGMENTS

We are grateful to Matthias Wieneke and Prof. Dr. Armin Dadgar (Institut für Physik, Otto-von-Guericke-Universität Magdeburg, Germany) for providing the *a*-GaN thin film sample and to ams-OSRAM International GmbH, Regensburg for providing the *c*-GaN thin film sample. We thank Gabriele Benndorf for the photoluminescence characterization of the GaN and ZnO samples. The authors thank Holger von Wenckstern from the Combinatorial Epitaxy Group at the Felix Bloch Institute for Solid State Physics for valuable discussions about the optical and electrical properties of ZnO. This work was funded by the German Federal Ministry of Education and Research (Grant No. 05K19OL1). Furthermore, we acknowledge DESY (Hamburg, Germany), a member of the Helmholtz Association HGF, for the provision of experimental facilities. This research was carried out at beamline P65 of PETRA III under proposals II-20200005 and I-20220601.

DATA AVAILABILITY

The data that support the findings of this paper are not publicly available upon publication because it is not technically feasible and/or the cost of preparing, depositing, and hosting the data would be prohibitive within the terms of this research project. The data are available from the authors upon reasonable request.

[1] D. Grandjean, E. Coutino-Gonzalez, N. T. Cuong, E. Fron, W. Baekelant, S. Aghakhani, P. Schlexer, F. D'Acapito, D. Banerjee, M. B. J. Roeffaers, M. T. Nguyen, J. Hofkens, and P. Lievens, Origin of the bright photoluminescence of few-atom silver clusters confined in LTA zeolites, Science **361**, 686 (2018).

[2] G. Fevola *et al.*, 3D and multimodal x-ray microscopy reveals the impact of voids in CIGS solar cells, Adv. Sci. **11**, 2301873 (2024).

[3] C. T. Plass, V. Bonino, M. Ritzer, L. R. Jäger, V. Rey-Bakaikoa, M. Hafermann, J. Segura-Ruiz, G. Martínez-Criado, and C. Ronning, Spatially resolved dynamics of cobalt color centers in ZnO canowires, Adv. Sci. **10**, 2205304 (2023).

[4] T. K. Sham, Photon-in/photon-out spectroscopic techniques for materials analysis: Some recent developments, Adv. Mater. **26**, 7896 (2014).

[5] A. Rogalev and J. Goulon, X-ray excited optical luminescence spectroscopies, in *Chemical Applications of Synchrotron Radiation, Part II: X-ray Applications*, edited by T. K. Sham (World Scientific, Singapore, 2002), pp. 707–760.

[6] C. J. Dolan, D. N. Cakan, R. E. Kumar, M. Kodur, J. R. Palmer, Y. Luo, B. Lai, and D. P. Fennig, Scanning x-ray excited optical luminescence of heterogeneity in halide perovskite alloys, J. Phys. D: Appl. Phys. **56**, 034002 (2023).

[7] N. Ortiz Hernández, S. Parchenko, J. R. L. Mardegan, M. Porer, E. Schierle, E. Weschke, M. Ramakrishnan, M. Radovic, J. A. Heuver, B. Noheda, N. Daffé, J. Dreiser, H. Ueda, and U. Staub, Magnetic field dependent cycloidal rotation in pristine and Ge-doped $CoCr_2O_4$, Phys. Rev. B **103**, 085123 (2021).

[8] R. J. Green, T. Z. Regier, B. Leedahl, J. A. McLeod, X. H. Xu, G. S. Chang, E. Z. Kurmaev, and A. Moewes, Adjacent Fe-vacancy interactions as the origin of room temperature ferromagnetism in $(In_{1-x}Fe_x)_2O_3$, Phys. Rev. Lett. **115**, 167401 (2015).

[9] M. Ishii, Y. Tanaka, T. Ushikawa, S. Komuro, T. Morikawa, and Y. Aoyagi, Site-selective x-ray absorption fine structure analysis of an optically active center in Er-doped semiconductor thin film using x-ray-excited optical luminescence, Appl. Phys. Lett. **78**, 183 (2001).

[10] X. T. Zhou, F. Heigl, J. Y. P. Ko, M. W. Murphy, J. G. Zhou, T. Regier, R. I. R. Blyth, and T. K. Sham, Origin of luminescence from Ga_2O_3 nanostructures studied using x-ray absorption and luminescence spectroscopy, Phys. Rev. B **75**, 125303 (2007).

[11] T. K. Sham, D. T. Jiang, I. Coulthard, J. W. Lorimer, X. H. Feng, K. H. Tan, S. P. Frigo, R. A. Rosenberg, D. C. Houghton, and B. Bryskiewicz, Origin of luminescence from porous silicon deduced by synchrotron-light-induced optical luminescence, Nature (London) **363**, 331 (1993).

[12] L. Soderholm, G. K. Liu, M. R. Antonio, and F. W. Lytle, X-ray excited optical luminescence (XEOL) detection of x-ray absorption fine structure (XAFS), J. Chem. Phys. **109**, 6745 (1998).

[13] F. Boscherini, X-ray absorption fine structure in the study of semiconductor heterostructures and nanostructures, in *Characterization of Semiconductor Heterostructures and Nanostructures*, edited by C. Lamberti (Elsevier, Amsterdam, 2008).

[14] A. Bianconi, D. Jackson, and K. Monahan, Intrinsic luminescence excitation spectrum and extended x-ray absorption fine structure above the K edge in CaF_2, Phys. Rev. B **17**, 2021 (1978).

[15] S. Emura, T. Moriga, J. Takizawa, M. Nomura, K. R. Bauchspiess, T. Murata, K. Harada, and H. Maeda, Optical-luminescence yield spectra produced by x-ray excitation, Phys. Rev. B **47**, 6918 (1993).

[16] B. H. Lin, H. Y. Chen, S. C. Tseng, J. X. Wu, B. Y. Chen, C. Y. Lee, G. C. Yin, S. H. Chang, M. T. Tang, and W. F. Hsieh, Probing the exciton-phonon coupling strengths of O-polar and Zn-polar ZnO wafer using hard x-ray excited optical luminescence, Appl. Phys. Lett. **109**, 192104 (2016).

[17] B. H. Lin, Y. C. Wu, J. F. Lee, M. T. Tang, and W. F. Hsieh, Polarization-dependent XEOL: Comparison of peculiar near-band-edge emission of non-polar a-plane GaN and ZnO wafers, Appl. Phys. Lett. **114**, 091102 (2019).

[18] G. Martinez-Criado, B. Alen, A. Homs, A. Somogyi, C. Miskys, J. Susini, J. Pereira-Lachataignerais, and J. Martınez-Pastor, Scanning x-ray excited optical luminescence microscopy in GaN, Appl. Phys. Lett. **89**, 221913 (2006).

[19] S. Levcenko, R. Biller, T. Pfeiffelmann, K. Ritter, H. H. Falk, T. Wang, S. Siebentritt, E. Welter, and C. S. Schnohr, High-resolution XEOL spectroscopy setup at the x-ray absorption spectroscopy beamline P65 of PETRA III, J. Synchrotron Radiat. **29**, 1209 (2022).

[20] E. Welter, R. Chernikov, M. Herrmann, and R. Nemausat, A beamline for bulk sample x-ray absorption spectroscopy at the high brilliance storage ring PETRA III, AIP Conf. Proc. **2054**, 040002 (2019).

[21] E. M. Kaidashev, M. Lorenz, H. von Wenckstern, A. Rahm, H. C. Semmelhack, K. H. Han, G. Benndorf, C. Bundesmann, H. Hochmuth, and M. Grundmann, High electron mobility of epitaxial ZnO thin films on c-plane sapphire grown by multistep pulsed-laser deposition, Appl. Phys. Lett. **82**, 3901 (2003).

[22] M. A. Reshchikov, H. Morkoc, B. Nemeth, J. Nause, J. Xie, B. Hertog, and A. Osinsky, Luminescence properties of defects in ZnO, Phys. B (Amsterdam, Neth.) **401**, 358 (2007).

[23] J. D. McNamara, N. M. Albarakati, and M. A. Reshchikov, Abrupt and tunable quenching of photoluminescence in ZnO, J. Lumin. **178**, 301 (2016).

[24] See Supplemental Material at http://link.aps.org/supplemental/10.1103/PhysRevResearch.7.023066 for XEOL data and results of the c-ZnO bulk samples ($d = 251$, 188, and 110 μm) and a-GaN samples ($d = 485$ and 2.7 μm), and the numerical results of the XANES spectrum distortions associated with the uncertainty for the input parameters of the calibration curve method.

[25] R. Heitz, A. Hoffmann, and I. Broser, Fe^{3+} center in ZnO, Phys. Rev. B **45**, 8977 (1992).

[26] S. Müller, M. Zhou, Q. Li, and C. Ronning, Intra-shell luminescence of transition-metal-implanted zinc oxide nanowires, Nanotechnology **20**, 135704 (2009).

[27] H. von Wenckstern, H. Schmidt, M. Grundmann, M. W. Allen, P. Miller, R. J. Reeves, and S. M. Durbin, Defects in hydrothermally grown bulk ZnO, Appl. Phys. Lett. **91**, 022913 (2007).

[28] H. von Wenckstern, H. Schmidt, C. Hanisch, M. Brandt, C. Czekalla, G. Benndorf, G. Biehne, A. Rahm, H. Hochmuth, M. Lorenz, and M. Grundmann, Homoepitaxy of ZnO by pulsed-laser deposition, Phys. Status Solidi RRL **1**, 129 (2007).

[29] M. R. Wagner, G. Callsen, J. S. Reparaz, J. H. Schulze, R. Kirste, M. Cobet, I. Ostapenko, S. Rodt, C. Nenstiel, M. Kaiser, A. Hoffmann, A. V. Rodina, M. R. Phillips, S. Lautenschlager, S. Eisermann, and B. K. Meyer, Bound excitons in ZnO:

Structural defect complexes versus shallow impurity centers, Phys. Rev. B **84**, 035313 (2011).
[30] M. A. Reshchikov, Measurement and analysis of photoluminescence in GaN, J. Appl. Phys. **129**, 121101 (2021).
[31] M. A. Reshchikov, P. Ghimire, and D. O. Demchenko, Magnesium acceptor in gallium nitride. I. Photoluminescence from Mg-doped GaN, Phys. Rev. B **97**, 205204 (2018).
[32] M. A. Reshchikov, O. Andrieiev, M. Vorobiov, B. McEwen, S. Shahedipour-Sandvik, D. Ye, and D. O. Demchenko, Stability of the C_NH_i complex and the blue luminescence band in GaN, Phys. Status Solidi B **258**, 2100392 (2021).
[33] L. Tröger, D. Arvanitis, K. Baberschke, H. Michaelis, U. Grimm, and E. Zschech, Full correction of the self-absorption in soft-fluorescence extended x-ray-absorption fine structure, Phys. Rev. B **46**, 3283 (1992).
[34] S. Eisebitt, T. Boske, J.-E. Rubensson, and W. Eberhardt, Determination of absorption coefficients for concentrated samples by fluorescence detection, Phys. Rev. B **47**, 14103 (1993).
[35] P. Pfalzer, J.-P. Urbach, M. Klemm, S. Horn, M. L. denBoer, A. I. Frenkel, and J. P. Kirkland, Elimination of self-absorption in fluorescence hard-x-ray absorption spectra, Phys. Rev. B **60**, 9335 (1999).
[36] C. H. Booth and F. Bridges, Improved self-absorption correction for fluorescence measurements of extended x-ray absorption fine-structure, Phys. Scr. T **115**, 202 (2005).
[37] R. M. Trevorah, C. T. Chantler, and M. J. Schalken, Solving self-absorption in fluorescence, IUCrJ **6**, 586 (2019).
[38] A. Iida and T. Noma, Correction of the self-absorption effect in fluorescence x-ray absorption fine structure, Jpn. J. Appl. Phys. **32**, 2899 (1993).
[39] A. P. Reddy and A. Mehta, Characterization & correction of self-absorption distortion in XANES, CUSJ **14**, 9 (2020).
[40] B. Ravel and M. Newville, ATHENA, ARTEMIS, HEPHAESTUS: Data analysis for x-ray absorption spectroscopy using IFEFFIT, J. Synchrotron Radiat. **12**, 537 (2005).
[41] J. A. Spencer, A. L. Mock, A. G. Jacobs, M. Schubert, Y. Zhang, and M. J. Tadjer, A review of band structure and material properties of transparent conducting and semiconducting oxides: Ga_2O_3, Al_2O_3, In_2O_3, ZnO, SnO_2, CdO, NiO, CuO, and Sc_2O_3, Appl. Phys. Rev. **9**, 011315 (2022).
[42] O. Ambacher, Growth and applications of group III-nitrides, J. Phys. D: Appl. Phys. **31**, 2653 (1998).
[43] H. B. DeVore, Spectral distribution of photoconductivity, Phys. Rev. **102**, 86 (1956).
[44] R. K. Ahrenkiel, *Minority Carriers in III-V Semiconductors: Physics and Applications*, edited by R. K. Ahrenkiel and M. S. Lundstrom (Academic, San Diego, CA, 1993), pp. 1–150.
[45] K. Lawniczak-Jablonska, T. Suski, I. Gorczyca, N. E. Christensen, K. E. Attenkofer, R. C. C. Perera, E. M. Gullikson, J. H. Underwood, D. L. Ederer, and Z. Liliental-Weber, Electronic states in valence and conduction bands of group-III nitrides: Experiment and theory, Phys. Rev. B **61**, 16623 (2000).
[46] J. H. Guo, L. Vayssieres, C. Persson, R. Ahuja, B. Johansson, and J. Nordgren, Polarization-dependent soft-x-ray absorption of highly oriented ZnO microrodarrays, J. Phys.: Condens. Matter **14**, 6969 (2002).
[47] M. Rebien, W. Henrion, M. Bär, and Ch.-H. Fischer, Optical properties of ZnO thin films: Ion layer gas reaction compared to sputter deposition, Appl. Phys. Lett. **80**, 3518 (2002).
[48] G. E. Jellison, Jr. and L. A. Boatner, Optical functions of uniaxial ZnO determined by generalized ellipsometry, Phys. Rev. B **58**, 3586 (1998).
[49] S. Shokhovets, L. Kirste, J. H. Leach, S. Krischok, and M. Himmerlich, Anisotropic optical constants, birefringence, and dichroism of wurtzite GaN between 0.6 eV and 6 eV, J. Appl. Phys. **122**, 045706 (2017).
[50] O. Lopatiuk, L. Chernyak, A. Osinsky, J. Q. Xie, and P. P. Chow, Lithium-related states as deep electron traps in ZnO, Appl. Phys. Lett. **87**, 214110 (2005).
[51] O. Lopatiuk-Tirpak, L. Chernyak, F. X. Xiu, J. L. Liu, S. Jang, F. Ren, S. J. Pearton, K. Gartsman, Y. Feldman, A. Osinsky, and P. Chow, Studies of minority carrier diffusion length increase in *p*-type ZnO:Sb, J. Appl. Phys. **100**, 086101 (2006).
[52] L. Chernyak, A. Osinsky, H. Temkin-H, J. W. Yang, Q. Chen, and M. A. Khan, Electron beam induced current measurements of minority carrier diffusion length in gallium nitride, Appl. Phys. Lett. **69**, 2531 (1996).
[53] N. Ino and N. Yamamoto, Low temperature diffusion length of excitons in gallium nitride measured by cathodoluminescence technique, Appl. Phys. Lett. **93**, 232103 (2008).
[54] R. L. Weiher and W. C. Tait, Mixed-mode excitons in the photoluminescence of zinc oxide-reabsorption and exciton diffusion, Phys. Rev. B **5**, 623 (1972).
[55] T. Schmidt, K. Lischka, and W. Zulehner, Excitation-power dependence of the near-band-edge photoluminescence of semiconductors, Phys. Rev. B **45**, 8989 (1992).
[56] T. Onuma, N. Sakai, T. Igaki, T. Yamaguchi, A. A. Yamaguchi, and T. Honda, Comparative study of surface recombination in hexagonal GaN and ZnO surfaces, J. Appl. Phys. **112**, 063509 (2012).
[57] R. A. Rosenberg, Defect specific luminescence dead layers in CdS and CdSe, Can. J. Chem. **95**, 1141 (2017).
[58] D. Salomon, A. Messanvi, J. Eymery, and G. Martínez-Criado, Silane-induced N-polarity in wires probed by a synchrotron nanobeam, Nano Lett. **17**, 946 (2017).
[59] C. Ossig, C. Strelow, J. Flügge, A. Kolditz, J. Siebels, J. Garrevoet, K. Spiers, M. Seyrich, D. Brückner, N. Pyrlik, J. Hagemann, F. Seiboth, A. Schropp, R. Carron, G. Falkenberg, A. Mews, C. G. Schroer, T. Kipp, and M. E. Stuckelberger, Four-fold multi-modal x-ray microscopy measurements of a Cu(In, Ga)Se_2 solar cell, Materials **14**, 228 (2021).
[60] C. Ossig, C. Strelow, J. Flügge, S. Patjens, J. Garrevoet, K. Spiers, J. L. Barp, J. Hagemann, F. Seiboth, M. De Bastiani, E. Aydin, F. H. Isikgor, S. De Wolf, G. Falkenberg, A. Mews, C. G. Schroer, T. Kipp, and M. E. Stuckelberger, Novel detection scheme for temporal and spectral x-ray optical analysis: Study of triple-cation perovskites, PRX Energy **3**, 023011 (2024).